Nearshore Bathymetry Based on ICESat-2 and Multispectral Images: Comparison Between Sentinel-2, Landsat-8, and Testing Gaofen-2

Xiaohan Zhang, Yifu Chen, Yuan Le, Dongfang Zhang, Qian Yan, Yusen Dong, Wei Han, and Lizhe Wang, *Fellow, IEEE*

***Abstract*—Accurate bathymetric maps are essential to understand marine and coastal ecosystems. With the development of satellite and sensor technology, satellite-derived bathymetry (SDB) has been widely used to measure the depth of nearshore waters. Employment of physics-based methods requires a series of optical parameters of the water column and seafloor, which limits the application of these methods to shallow-water bathymetry. Due to convenience, low costs, and high efficiency, empirical methods based on *in situ* measurements and satellite imagery are increasingly used for nearshore bathymetry. These measurements are required to calibrate empirical models, so that reasonable accuracy can be achieved. The Ice, Cloud, and Land Elevation Satellite-2 (ICESat-2), equipped with the advanced topographic laser altimeter system, provides a novel opportunity for nearshore bathymetry. Using the new measurement strategy of photon counting, ICESat-2 can provide accurate bathymetric points from spaceborne observations, which can be used in place of *in situ* water depth data. In this study, ICESat-2 bathymetric points and multispectral images were used to train four typical models and produce bathymetric maps for Shanhu Island, Ganquan Island, and Lingyang Reef in the Xisha Islands of China. We evaluated the bathymetric results by comparing them with reference depth data from airborne light detection and ranging. All models had a satisfactory accuracy, as well as multimodel and multisource image consistency. With the ICESat-2 bathymetric points, SDB is no longer limited by *in situ* measurements. Hence, this approach could be extended to a larger scale to obtain nearshore bathymetric maps of coastal areas, surrounding islands, and reefs using free and open-access satellite data.**

***Index Terms*—Empirical models, ice cloud and land elevation satellite-2 (ICESat-2), multispectral images, nearshore, satellite-derived bathymetry (SDB).**

Manuscript received July 2, 2021; revised October 22, 2021 and January 26, 2022; accepted February 12, 2022. Date of publication February 23, 2022; date of current version March 29, 2022. This work was supported by the National Natural Science Foundation of China under Grant 41925007, Grant U1711266, and Grant 42171373. *(Corresponding author: Lizhe Wang.)*

Xiaohan Zhang, Yifu Chen, Dongfang Zhang, Yusen Dong, Wei Han, and Lizhe Wang are with the School of Computer Science, China University of Geosciences, Wuhan 430074, China, and also with the Hubei Key Laboratory of Intelligent Geo-Information Processing, China University of Geosciences, Wuhan 430074, China (e-mail: zxh_cug@163.com; stein_syf@foxmail.com; zhangdongfang@cug.edu.cn; ysdong@cug.edu.cn; weihan@cug.edu.cn; lizhe.wang@gmail.com).

Yuan Le and Qian Yan are with the School of Geography and Information Engineering, China University of Geosciences, Wuhan 430074, China (e-mail: leyuan@cug.edu.cn; 604119082@qq.com).

Digital Object Identifier 10.1109/JSTARS.2022.3153681

I. Introduction

DETAILED and accurate nearshore bathymetry is critical for a variety of applications, including offshore navigation, ocean research, and marine spatial management [1], [2]. With the expansion of human activities in coastal and marine areas, there is a growing need to investigate the topography and physical features of the seafloor [3]. The main objective of nearshore bathymetry is to assess shallow water regions around coastal zones, straits, or islands, and to shrink the nearshore data gap termed the "white ribbon" by the hydrographic community [4]–[6].

In recent decades, a series of techniques have been developed to measure and estimate water depth. Two of the most widely used techniques: 1) single or multibeam echo-sounding; and 2) airborne light detection and ranging (LiDAR), and have been successfully applied in various coastal and marine regions [7]–[10]. Echo-sounding hydrographic survey techniques acquire high-accuracy bathymetric data, which are difficult to collect in areas of shallow water or near reefs, rocks, and similar hazards [11]. The airborne LiDAR bathymetry (ALB) system with a 532-nm laser beam is widely used in nearshore applications, but it has low efficiency and high costs. Furthermore, it is easily affected by weather and environmental conditions [12]. One method of solving these problems uses satellite-derived bathymetry (SDB).

SDB is based on remote sensing images and *in situ* measurements, and it is a cost-effective means of obtaining bathymetric maps for a wide area. In recent years, spaceborne and airborne sensors with different spatial and spectral resolutions, such as LandSat-8, Sentinel-2, WorldView-2, QuickBird, IKONOS, and AVIRIS, have been used successfully for nearshore bathymetry [3], [13]–[17]. Two main methods are used to perform SDB: 1) empirical; and 2) physics-based model inversion approaches [18]–[21]. Physics-based approaches can be applied without *in situ* water depth measurements, but they are more challenging to implement and computationally demanding. Empirical approaches are more common, as they offer a practical way to derive bathymetry from optical remote sensing data [22], [23]. Water depth has an empirical relationship with light attenuation in water that may appear in spectral changes; however, factors, such as atmospheric conditions, water transparency, bottom type, and surface waves, can affect the relationship between

the surface reflectance and water depth [24]. Consequently, *in situ* measurements are required to calibrate the empirical relationship so that reasonable accuracy can be achieved. Currently, *in situ* water depth measurements in nearshore areas are lacking, but the recently launched Ice, Cloud, and Land Elevation Satellite-2 (ICESat-2) provides a novel opportunity for nearshore bathymetry. ICESat-2 is the first spaceborne laser altimeter to be equipped with the advanced topographic laser altimeter system (ATLAS). ATLAS uses a green laser (532 nm) with 10 000 pulses per second (10 kHz), a footprint 17 m in diameter, and an along-track sampling interval of 0.7 m [25]. It has three laser beams along the track, and the distance between adjacent beams is approximately 3.3 km. Each beam is divided into strong and weak sub-beams. The energy of the strong sub-beam is approximately four times than that of the weak sub-beam, and the distance between them is 90 m [26]. Previous studies have suggested that nearshore bathymetry based on ICESat-2 is possible, and ICESat-2 can measure water depths up to 38 m in optically clear waters [27], [28]. Even if the spacing between the beam pairs is too wide to generate high-resolution bathymetric results, water depth profiles derived from ICESat-2 can be used to seed SDB. Nearshore bathymetry based on ICESat-2 and multispectral images have been investigated only in a few locations [24], [29]. There is still a lack of global-scale research on SDB calculated using a combination of ICESat-2 data and remote sensing images.

In this study, bathymetric maps of two islands and a reef located in the Xisha Islands were produced by combining ICESat-2 data and satellite multispectral images. First, raw ICESat-2 data were processed through a high-accuracy filtering method oriented to bathymetry. For each extracted seafloor photon, errors arising from the refraction effect in the water column were corrected. Second, the bathymetry points of ICESat-2 were used as *in situ* measurements to train the four models: 1) the linear; 2) band ratio; 3) support vector regression (SVR); and 4) random forest (RF) models. In addition, the SDB results were compared with the ALB reference data. The aims of this study are summarized as follows.

1) Evaluate the altimetry and bathymetry accuracy of ICESat-2 data.
2) Validate and estimate the accuracy of SDB results based on ICESat-2 data and satellite multispectral images.
3) Compare the bathymetric results for different sources of multispectral images.

The rest of this article is organized as follows. Section II presents related work. Section III describes the estimation methods and data, including data processing procedures used in the experiment. Section IV contains a description of results and an analysis of the experimental results. Section V discusses the errors caused by different settings in the experiment. Finally, Section VI concludes this article.

II. Methods of Satellite-Derived Bathymetry

SDB based on remote sensing images and *in situ* measurements is the commonly used method of obtaining bathymetric maps, which can be classified into following two categories according to the principle [30].

1) Classical methods require to determining the unknown parameters in known formula by statistics and experience, in order to determine the relationship between image information and depth.
2) Machine learning methods require a large number of *in situ* data to train the model and obtain the water depth.

The abovementioned two methods require a large amount of *in situ* data to solve the unknown parameters or build the model.

A. Classical Methods

Currently, the widely used bathymetry classical is the linear band model and band ratio model. Lyzenga [31] proposed a single-band water depth inversion method and a multiband linear combination water depth inversion method based on the assumption of clear water. Many scholars have improved the method to adapt to more complex water depth detection scenarios. Stumpf [19] aimed at the linear method in turbid waters. The problem of poor effect is improved, and a band ratio method, suitable for turbid waters, is proposed. Compared with the linear method, the band ratio method reduces the parameters that need to be adjusted and at the same time exhibits stronger stability. Liu *et al.* [32] proposed an adaptive blended algorithm approach to improve the method proposed by Stumpf, which significantly improved the accuracy of the estimate of water depth. Cao *et al.* [33] used the band ratio method to estimate the depth of the St. Croix area. Forfinski-Sarkozi and Parrish [34] used the Stumpf's method to fuse single-photon data with Landsat-8 data to draw the Keweenaw Bay nearshore water depth map. Ma *et al.* [24] used the abovementioned two classic methods to fuse single-photon data as *in situ* data with Sentinel-2 images, and the map of water depth map was drawn on the shallow water area of Acklins Island.

However, classical methods require certain empirical theories to determine unknown parameters, so there are certain limitations in their used.

B. Machine Learning Methods

In the research of water depth inversion, the most commonly used machine learning methods include SVR [35], RF [36], etc. The principle of machine learning methods to estimate water depth is mainly by constructing a nonlinear relationship between surface reflectivity and water depth. Compared with the classic method, the machine learning method does not require any empirical knowledge of attenuation, water quality, or bottom type, and has wider applicability. Tonion *et al.* [37] compared the performance of three different ML algorithms in predicting sea depth, the RF root mean square error (rmse) was 0.228, but the content error was very serious. Zhang *et al.* [38] used Sentinel-2 and SVR methods and corrected by residual interpolation. The estimated water depth reduces the rmse by 0.3 m. Thomas *et al.* [39] developed one of the first fully space-based open source approaches to measure nearshore bathymetry in optically shallow waters. Albright and Glennie [29] used the fusion data of Sentinel-2 and ICEsat-2 as a dataset and used the SVR method

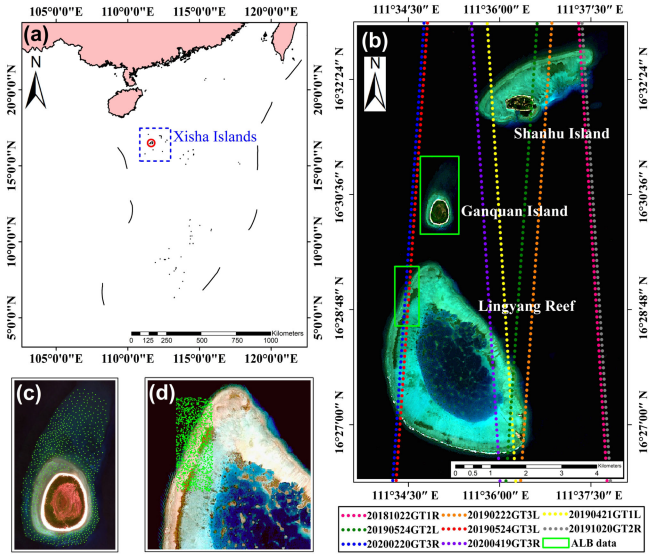

Fig. 1. (a) Location of the study area. (b) ICESat-2 trajectories used in this study, where dotted lines of different colors represent data acquired on different dates and the two green rectangles correspond to the distribution of the reference water depth acquired by the airborne LiDAR and illustrated in detail in (c) and (d).

to train a water depth inversion model. The rmse of the water depth is estimated to be only 0.13 m.

Due to the limitation of the measurement area, the abovementioned method can only complete the water depth estimation in the area with *in situ* data. Due to its own characteristics, ICESat-2 satellite can provide bathymetric points on a global scale, which well solves the regional limitation of *in situ* data measurement. The limitation of the development of the ICESat-2 data processing method makes the application of ICESat-2 data in depth estimation and mapping less. Therefore, this article evaluates the ICESat-2 data processing method of Chen *et al.* [40], and then applies it to shallow water detection. The performance of different water depth estimation methods in the same image and the influence of different image resolutions on water depth detection methods are explored at the same time.

III. Materials and Methods

A. Study Area

The Xisha Islands (also known as the Paracel Islands) are a group of islands, reefs, banks, and other maritime features in the South China Sea [see Fig. 1(a)]. This archipelago includes approximately 130 small coral islands and reefs, grouped into the northeastern Dexuan Islands and western Yongle Islands (also known as Amphitrite Group and Crescent Group, respectively) [41]. They are distributed over an area of 15 000 km^2, with a land area of 7.75 km^2. Our study area is in the Yongle Islands, including Ganquan Island, Shanhu Island, and Lingyang Reef [see Fig. 1(b)]. Shanhu Island is located in the northwestern Yongle Islands. It is oval in shape, 900-m long from east to west, 450-m wide from north to south, and covers an area of 0.31 km^2. Ganquan Island lies to the west of the Yongle Islands, at 16°30'N, 111°35'E. It is a lime sand island that has grown from coral reefs, and it has a land area of 0.3 km^2. The Lingyang Reef is a small reef to the southwest of the Yongle Islands, it is 12 km from north to south and 4 km from east to west. This small atoll is approximately triangular and has no access to the sea or large exposed areas during low tide.

TABLE I
Descriptions of the Atlas Trajectories Used in This Study

Island(s) in transit	ATLAS Dataset	Trajectory used	Acquisition time (UTC)
Lingyang Reef	20190524	GT3L	09:31
	20200220	GT3R	20:33
Lingyang Reef and Shanhu Island	20190222	GT3L	13:51
	20190421	GT1L	22:58
	20190524	GT2L	09:31
	20200419	GT3R	05:41
Shanhu Island	20181022	GT1R	07:42
	20191020	GT2R	14:22

B. ATL03 Data

ATL03 is the ICESat-2 Level-2 global geolocated photon dataset, and includes six "gtx" groups (GT1L, GT1R, GT2L, GT2R, GT3L, and GT3R), each containing segments for one ground track. Each photon in each group has a latitude, longitude, and elevation based on the WGS84 ellipsoid benchmark [42]. To improve the measurement accuracy of the ATLAS and expand its applicable range, a set of geophysical corrections are applied to the ATL03 data, including solid Earth tide, dynamic atmospheric, and inverted barometer effect corrections [43], [44]. The detector is extremely sensitive, so the raw photon data in the ATL03 dataset are very noisy, especially during the day due to solar activity. Thus, a "confidence" parameter, numbered 0–4, is assigned to each photon in ATL03 to classify it as either a "likely signal" or "noise" [24]. In this study, eight ATL03 data files acquired between February 2019 and April 2020 were downloaded from the Goddard Earth Sciences Data and Information Services Center[1] as shown in Table I. Six ground trajectories that passed through the Lingyang Reef were selected [see Fig. 1(b)]. Two adjacent trajectories: 1) 20190524GT3L; and 2) 20200220GT3L, passed over the Lingyang Reef from north to southwest in parallel. The remaining four trajectories were distributed to the east of the Lingyang Reef in two pairs of parallel lines. The latitude, longitude, height, along-track distance, and confidence level of the raw photons in these trajectories were extracted from the ATL03 data and used for subsequent analysis.

C. Multispectral Remote Sensing Images

Three multispectral images, including the standard GaoFen-2 Level-1A product, standard Sentinel-2 multispectral instrument Level-1C product, and LandSat-8 operational land imager Level-1T product, were captured, resulting in a total of three images. To compare various inversion models, we selected images where the acquisition dates and times were as close as

[1][Online]. Available: https://earthdata.nasa.gov/eosdis/daacs/gesdisc

TABLE II
DESCRIPTION OF MULTISPECTRAL IMAGES

Satellite	Date	Data level	Acquisition Time (UTC)	Tide Height (m)
Sentinel-2	06/14/2017	L1C	03:04:34	0.54
Landsat-8	08/04/2017	L1GT	02:54:05	0.12
GaoFen-2	05/10/2017	L1A	03:36:14	0.27

possible. The information regarding the selected images is listed in Table II. Images with more than of 10% cloud cover were chosen. The images were geometrically projected on the universal transverse mercator/world geodetic system 84 system and preprocessed with atmospheric correction using the FLAASH model [45]. Furthermore, the solar glint effect was removed, and blue-, green-, and red-band data were extracted and used to construct the water depth inversion model using the ATLAS bathymetry data.

D. ALB Reference Data

The reference water depth data at Ganquan Island were acquired on January 9, 2013, using a scanned hydrographic operational airborne LiDAR system (SHOALS-3000, Canada). This ALB system uses a green laser (532 nm) with 3000 pulses per second (3 kHz), and it has a nominal bathymetry accuracy of 0.3 m [46]–[48]. The reference data at Lingyang Reef were obtained on July 16, 2018, using the Mapper 5000 ALB system developed by the Shanghai Institute of Optics and Fine Mechanics. This system uses a green laser (532 nm) with 5 kHz pulses, and it has a bathymetric accuracy of 0.23 m [49], [50]. The reference data distributions for Lingyang Reef and Ganquan Island are marked by the green rectangles in Fig. 1(b), and illustrated in detail in Fig. 1(c) and (d), respectively.

E. Methods

The ATL03 dataset containing the eight selected trajectories were first processed using a high-accuracy filtering method oriented to bathymetry. To automatically separate and detect the effective photon of the water surface and bottom, an ellipse filter was adopted using an adaptive variable ellipse-filtering method [40], where the size of the ellipse filter changes with the water depth and density distribution of the water-column photon. The proposed method has following five parts.

1) Slicing segments along the height direction and Gaussian curve fitting.
2) Separating the above-water, water surface, and water column photons.
3) Determining the initial parameters of the elliptical filter.
4) Establishing the relationship between the initial ellipse filter and the water-column photon density.
5) Detecting and fitting different types of effective photons detected.

The elevation of the extracted underwater photons was then corrected using a refraction correction method [51]. Tide correction is also essential for nearshore bathymetry using the ATLAS dataset and remote sensing images. Since there were no *in situ* measurements at the tide station, we conducted the tide correction using the tide model NAO.99b [52], a global ocean tide model that represents 16 major constituents with a spatial resolution of 0.5°. The constituents were estimated by assimilating five years of TOPEX/POSEIDON altimeter data into a barotropic hydrodynamical model. Model NAO.99b is characterized by reduced errors in shallow waters compared to other ocean tide models that use tide gauge data and collinear residual reduction tests [51].

To validate the correctness and reliability of the corrected seafloor photons for ATL03, their elevation was compared directly with the reference profile acquired by the ALB system.

Using the preprocessed multispectral images and ATL03 bathymetric points, we trained two empirical and two machine learning algorithms to generate bathymetric maps (see Table II). The most commonly used linear band and band ratio algorithms were developed by Lyzenga *et al.* [18], [31] and Stumpf *et al.* [19]. The following equations can, respectively, summarize these:

$$h_w = a_0 + \sum_{i=1}^{k} a_i \ln[R_w(\lambda_{\mathrm{i}}) - R_\infty(\lambda_{\mathrm{i}})] \tag{1}$$

$$h_w = m_0 \times \frac{\ln(n \times R_w(\lambda_{\mathrm{i}}))}{\ln(n \times R_w(\lambda_{\mathrm{j}}))} + m_1 \tag{2}$$

where h_w is the bathymetry derived from the multispectral image, $R_\infty(\lambda_i)$ is the above-water surface remote sensing reflectance for band *i*, and $R_\infty(\lambda_i)$ is the average deep water signal after atmospheric and sun glint corrections. Further, *n* is a fixed coefficient, generally set to 1000, which ensures that the logarithm is positive under any condition, and that the ratio produces a linear response with depth. Based on the *in situ* bathymetric points, the values of m_0, m_1, and a_i can be obtained by minimizing the difference between the estimated water depth and prior water depth. SVR is a machine learning algorithm that learns the nonlinear relationship between surface reflectance and water depth without empirical knowledge of the processes that would affect surface reflectance, such as attenuation, turbidity, or bottom type. The support vectors used for regression are determined by splitting the known pixel depths into uniformly distributed training/validation datasets, and the best regression fit is obtained using a kernel function. More details on the use of SVR for bathymetric inversion can be found elsewhere [53]. RFs for nonlinear regression are formed by growing trees that depend on a random vector, such that the tree predictor takes on numerical values as opposed to class labels [4]. The decision tree learning aims to create a model that predicts the value of a target variable based on several input variables [54]. To estimate the accuracy of the elevation of the ATL03 photons, the elevations of the extracted seafloor photons of trajectories 20190524GT3L and 20200220GT3L were directly compared with the ALB underwater profile. The bathymetric results used in this study, based on ATL03 bathymetric points and multispectral images, were further compared with the reference water depth data to validate the accuracy of the SDB results by calculating the coefficient of determination (R^2), bias, and rmse.

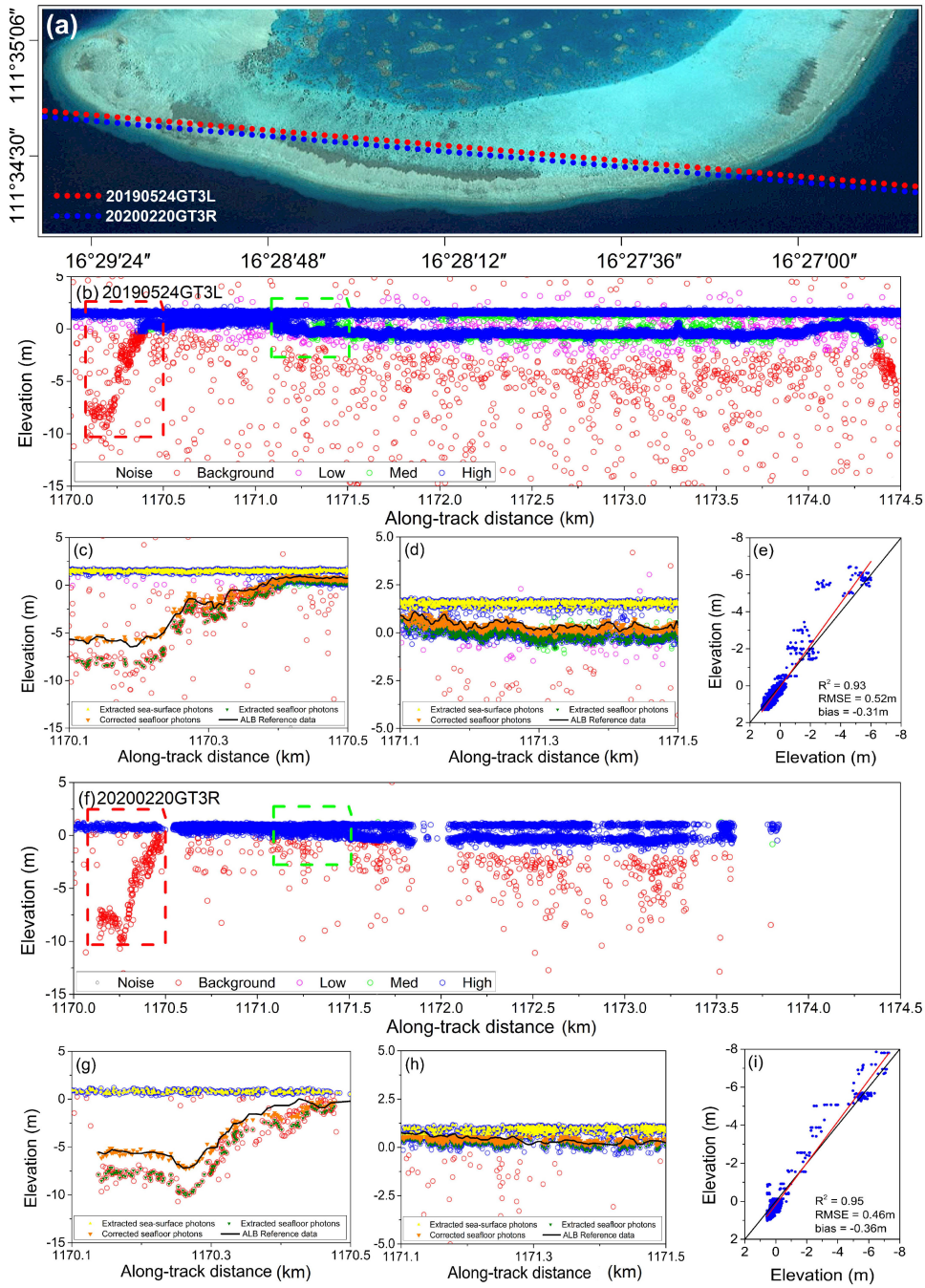

Fig. 2. ICESat-2 ground trajectories and raw points for 20190524GT3L and 20200220GT3R at the Lingyang Reef. Raw points distributed in shallow and deep waters are marked by red and green rectangles in (b) and (f). The filtered and fraction-corrected points are shown in detail in (c), (d), (g), and (h). The elevation relationships between corrected points and ALB reference data are shown in (e) and (f).

IV. Results

A. Detection of Signal Photons and Bathymetry With ATLAS

For two trajectories overlapping the area of the ALB reference data at Lingyang Reef (20190524GT3L and 20200220GT3R) [see Fig. 2(a)], the elevation of the corrected seafloor photons was compared with the ALB elevation profile to evaluate the altimetry accuracy of ICESat-2. As shown in Fig. 2(b) and (f), raw ATL03 data provided a confidence label for each photon. According to a visual assessment, some of the seafloor photons in shallow water and most of the sea surface photons were marked as "high" confidence. However, many seafloor photons were labeled as "background," especially those in the red rectangle in Fig. 2(b) and (f). After processing via the filtering method, the sea surface and seafloor photons were successfully extracted, and some of the photons with low density were excluded as outliers regardless of the confidence label [see Fig. 2(c) and (d) for 20190524GT3L, and Fig. 2(g) and (h) for 20200220GT3R]. After the refraction correction, the seafloor photons were in agreement with the reference ALB profile. In Fig. 2(e) and (i),

TABLE III
CALIBRATION RESULTS FOR THE FOUR MODELS WITH THREE REMOTE SENSING IMAGES

Models	Bandused	Shorthand	GaoFen-2		Sentinel-2		LandSat-8	
			R^2	RMSE(m)	R^2	RMSE(m)	R^2	RMSE(m)
LB	Blue, Green	LB_{BG}	0.69	1.16	0.88	0.93	0.89	0.91
	Blue, Red	LB_{BR}	0.64	1.26	0.57	1.81	0.53	1.88
	Green, Red	LB_{GR}	0.71	1.14	0.63	1.67	0.70	1.47
	Blue, Green, Red	LB_{BGR}	0.73	1.09	0.92	0.88	0.91	0.81
BR	Blue/Green	BR_{BG}	0.72	1.11	0.83	1.28	0.85	1.24
	Blue/Red	BR_{BR}	0.59	1.38	0.59	1.72	0.61	1.69
	Green/Red	BR_{GR}	0.68	1.19	0.62	1.61	0.66	1.57
	Blue, Green, Red	–	–	–	–	–	–	–
SVR	Blue, Green	SVR_{BG}	0.77	1.04	0.89	0.77	0.92	0.74
	Blue, Red	SVR_{BR}	0.69	1.20	0.48	1.70	0.80	1.18
	Green, Red	SVR_{GR}	0.75	1.08	0.75	1.18	0.82	1.12
	Blue, Green, Red	SVR_{BGR}	0.84	0.90	0.90	0.73	0.94	0.66
RF	Blue, Green	RF_{BG}	0.83	0.91	0.93	0.64	0.93	0.69
	Blue, Red	RF_{BR}	0.71	1.17	0.74	1.19	0.82	0.97
	Green, Red	RF_{GR}	0.83	0.93	0.76	1.15	0.83	0.95
	Blue, Green, Red	RF_{BGR}	0.85	0.84	0.93	0.64	0.94	0.65

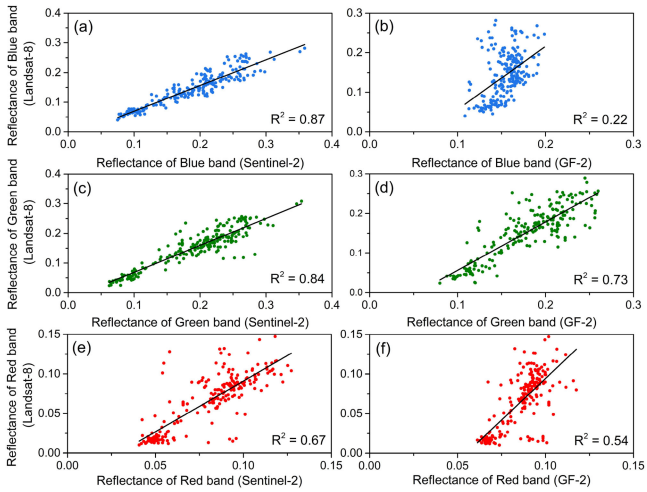

Fig. 3. Relationships between the reflectance values of the bands used. (a), (c), and (e) correspond to the relationship between the reflectance values of the blue, green, and red bands for LandSat-8 and Sentinel-2. (b), (d), and (f) correspond to the relationship between the reflectance values of the blue, green, and red bands for LandSat-8 and GaoFen-2.

the elevations of corrected seafloor photons showed a significant correlation with the ALB profile, that is, an R^2 of 0.93 and 0.95, and an rmse of 0.52 and 0.46 m for 20190524GT3L and 20200220GT3R, respectively. Despite the potential for temporal changes in the underwater topography during the acquisition of the ATL03 and ALB data, and the altimetry error of the ALB data (approximately 20 cm for seafloor points [55]), the elevation estimation of the corrected ATL03 photons was reliable and capable of describing the underwater topography in the study area.

B. Model Calibration of Different Band Selections

Three remote sensing images with various spatial resolutions were used to calibrate four inversion models to determine the effects of spatial resolution and band range on their performance. As given in Table III, for simplicity, the linear band model using blue and green bands was expressed as "LB_{BG}," and a similar notation was used for the other models. In general, all the models effectively retrieved the water depth of the study area ($R^2 = 0.48$–0.94 and rmse $= 0.64$–1.88 m). The dual-band models using blue and green bands performed better than those using blue and red, or green and red bands. After adding the reflectance of the red band to the LB, SVR, and RF models, the R^2 of the three-band models was slightly higher than that of the dual-band models using blue and green bands (GaoFen-2: 0.02–0.07, Sentinel-2: 0–0.04, and LandSat-8: 0.01–0.02). The strong absorption of the red band by water means that its bathymetric ability is extremely limited [56]. Moreover, from the perspective of model selection, the models based on the machine learning performed better than the empirical models.

The results in Table III demonstrate that the reflectance of the blue and green bands contains most of the water depth information in the Sentinel-2 and LandSat-8 images, but not in the GaoFen-2 images. For example, the R^2 of LB_{BG} was 0.69, which was very close to that of LB_{GR} (0.71); in contrast, the R^2 of LB_{BR} was 0.64. To further investigate the divergence between the GaoFen-2 images and the Sentinel-2 and Landsat-8 images, the reflectance images of Sentinel-2 and GaoFen-2 were resampled to a resolution of 30 m, using bilinear interpolation. The resampled reflectance was then compared to the reflectance of the LandSat-8 images. As shown in Fig. 3, the blue- and green-band reflectance values of the Sentinel-2 images showed significant correlation with those of the LandSat-8 images ($R^2 > 0.8$), and the red-band reflectance of the Sentinel-2 images showed moderate correlation with that of Landsat-8 images, with an R^2 of 0.67. This explains the similarity between the calibration results for Sentinel-2 and LandSat-8, especially when using the blue and green bands. In addition, the green- and red-band reflectance of the GaoFen-2 images showed moderate correlation with that of the LandSat-8 images, but the blue-band reflectance had a low correlation with the Landsat-8 images, with R^2 of 0.22. In our processing, the bathymetric capability of GaoFen-2's blue band was inferior to those of Sentinel-2 and LandSat-8. However, GaoFen-2 had the highest spatial resolution. Integration of the band comparison and model calibration results suggest that the blue and green bands should be considered when using the Sentinel-2 and LandSat-8 images for bathymetry calculations. Moreover, the green band should be considered when using GaoFen-2 images, due to its relatively weak bathymetric capability for the blue and red bands.

C. Accuracy and Precision of Bathymetric Estimates

The models with the highest calibration accuracy (LB_{BGR}, BR_{BG}, SVR_{BGR}, and RF_{BGR}) were selected to produce bathymetric maps for each multispectral image. Fig. 4(a)–(d) correspond to the bathymetric maps derived from the LB_{BGR}, BR_{BG}, SVR_{BGR}, and RF_{BGR} models for the GaoFen-2 images, respectively. Fig. 4(e)–(h) and (i)–(l) correspond to the bathymetric maps derived from the four models for the Sentinel-2 and LandSat-8 images, respectively. Although the water depth is affected by solar-induced background scattering, the performance of the satellite sensors, and changes in underwater topography [57], no significant differences were observed visually in the bathymetry results for the different images. The model consistency based on the Sentinel-2 and LandSat-8 images was

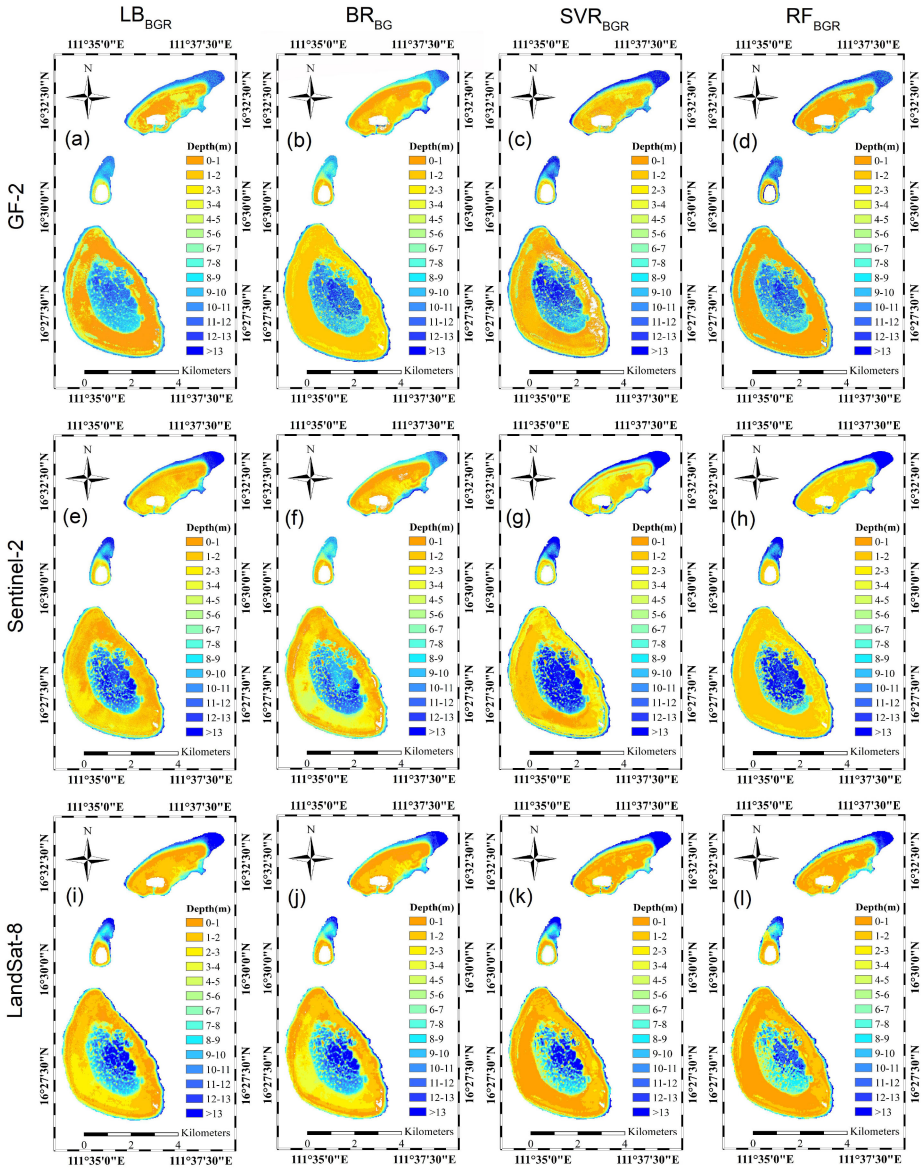

Fig. 4. Bathymetric maps for three multispectral images. (a)–(d), (e)–(h), and (i)–(l) correspond to bathymetric maps derived from the LB_{BGR}, BR_{BG}, SVR_{BGR}, and RF_{BGR} models and the GaoFen-2, Sentinel-2, and LandSat-8 images, respectively.

slightly better than that based on the GaoFen-2 images, due to the poor performance of GaoFen-2 in terms of blue-band reflectance.

The SDB results were validated using the *in situ* water depth for Ganquan Island and Lingyang Reef captured by the ALB system. The R^2, rmse, and bias values, as well as the regression lines between the estimated and *in situ* water depths, are shown in Fig. 5. There was a strong correlation between the SDB and ALB results. The bathymetric results based on the GaoFen-2 images showed the lowest accuracy, with an R^2 between 0.71 and 0.89 and rmse between 1.33 and 2.09 m at Ganquan Island, and R^2 between 0.71 and 0.75 and rmse between 1.03 and 1.41 m at Lingyang Reef. The retrieval results for Sentinel-2 and LandSat-8 were slightly better than those of GaoFen-2. There were no significant differences in the SDB results obtained using the four models, except for the GaoFen-2 images, where the SDB results with SVR_{BGR} and RF_{BGR} were better than those with LB_{BGR} and BR_{BG} when the ALB data from Ganquan Island were used for validation. Moreover, the correlation between the SDB and ALB results for Ganquan Island was slightly higher than that for Lingyang Reef. Although the reference water depth data in both places were acquired by the ALB systems, the data acquisition time, regional underwater topography, water depth distribution range, and process of tide correction affected the accuracy of the validation.

To further analyze the relationship between the estimated depth and reference water depth measured via ALB, the estimated and reference depths at Ganquan Island and Lingyang Reef were combined and then divided into several groups with a reference depth of 1 m as the interval. The R^2, rmse, and bias values for the estimated and reference water depths of the combined data are presented in Table IV. The bias at different

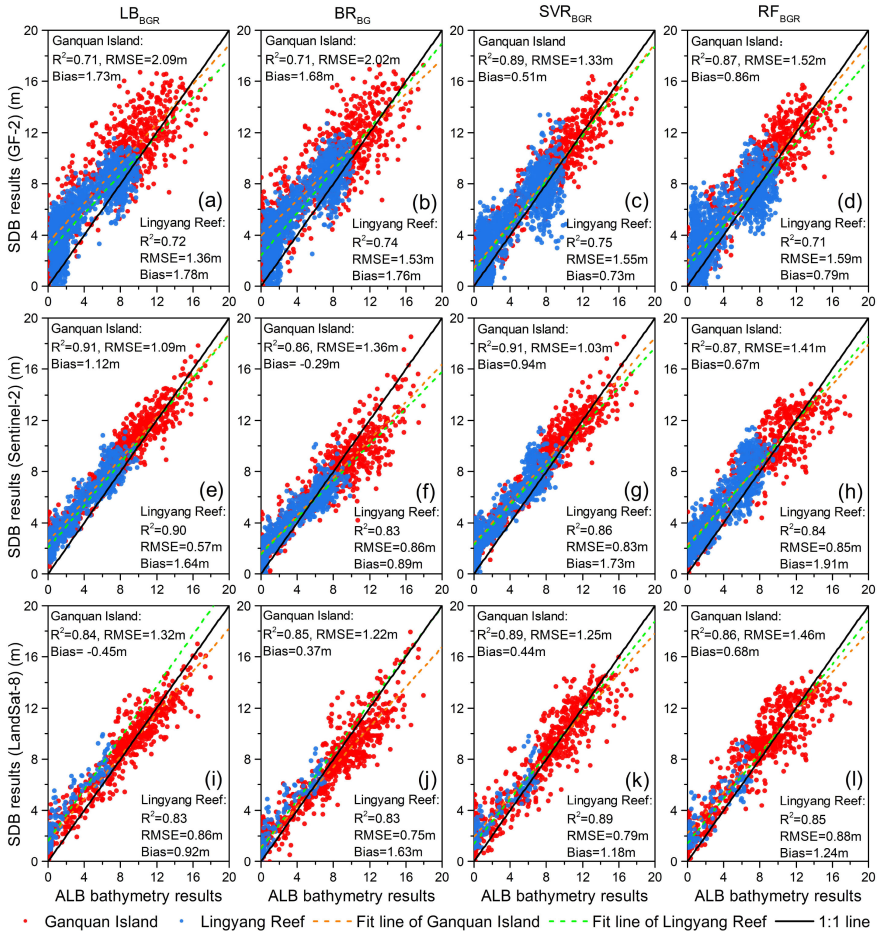

Fig. 5. Validation results based on the ALB reference water depth for three multispectral images. (a)–(d), (e)–(h), and (i)–(l) correspond to the results of the LB_{BGR}, BR_{BG}, SVR_{BGR}, and RF_{BGR} models for the GaoFen-2, Sentinel-2, and LandSat-8 images, respectively.

TABLE IV
VALIDATION RESULTS FOR THREE MULTISPECTRAL IMAGES WHEN THE ALB REFERENCE DATA OF GANQUAN ISLAND AND LINGYANG REEF ARE COMBINED

Images	LB_{BGR}			BR_{BG}			SVR_{BGR}			RF_{BGR}		
	R^2	RMSE (m)	Bias (m)	R^2	RMSE (m)	Bias (m)	R^2	RMSE (m)	Bias (m)	R^2	RMSE (m)	Bias (m)
GaoFen-2	0.71	1.63	1.77	0.72	1.61	1.74	0.84	1.43	0.67	0.81	1.58	0.81
Sentinel-2	0.90	0.94	1.49	0.87	1.12	0.66	0.89	0.97	1.51	0.88	1.31	1.36
LandSat-8	0.84	1.21	-0.29	0.86	1.23	0.70	0.91	1.15	0.64	0.88	1.33	0.83

intervals is shown in Fig. 6. As the water depth increased, the bias changed gradually from positive to negative, which demonstrates that the models often overestimate the water depth in extremely shallow regions, and underestimate it in deep areas. In extremely shallow areas less than 5-m deep, the sea wave, spindrift, and radiation of seafloor sediment may decrease the reliability of SDB results [58]. Moreover, the attenuation of light in water means that the water depth information included in optical remote sensing images also decreases gradually as the water depth increases [59].

Two ICESat-2 trajectories overlapping the eastern area of Shanhu Island, 20191020GT2R and 20181022GT1R, were not used in the model calibration. We used these trajectories to validate the SDB results for Shanhu Island. The results in Fig. 7 show that the correlations between the SDB results and ICESat-2 bathymetric points were slightly higher than those between the

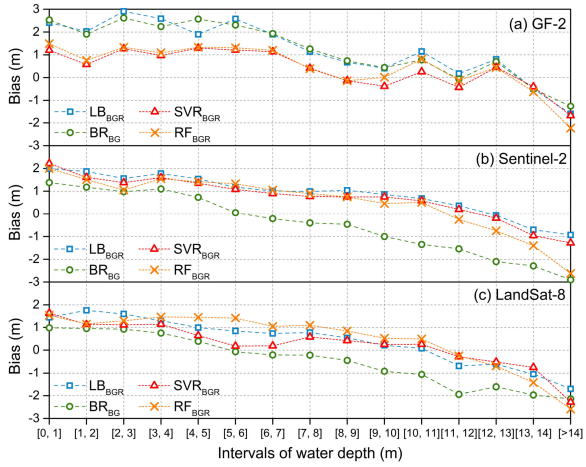

Fig. 6. Distribution of the bias for three multispectral images when the ALB reference data for Ganquan Island and Lingyang Reef are combined. The estimated water depth of the four models and reference data are separated into 1-m interval.

SDB and ALB results. For the GaoFen-2 images, the R^2 and rmse values for the bathymetric points of 20191020GT2R and SDB were between 0.73 and 0.87, and 0.87 and 1.42 m, respectively. In contrast, the values for the ALB and SDB results were

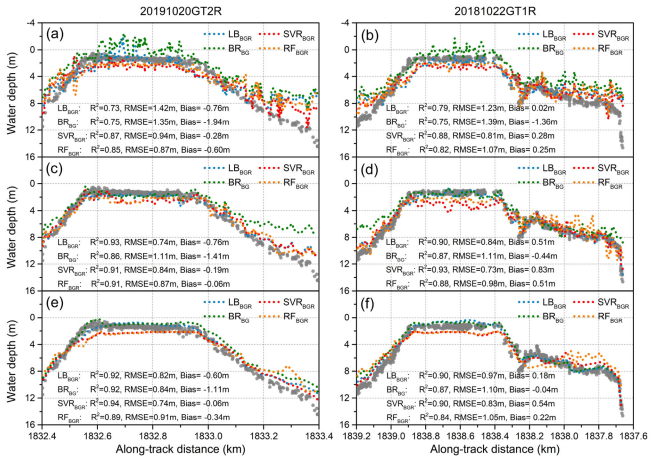

Fig. 7. Validation results based on 20191020GT2R and 20181022GT1R for three multispectral images. (a), (c), and (e) correspond to the results for the GaoFen-2, Sentinel-2, and LandSat-8 images, respectively. (b), (d), and (f) correspond to the results for the GaoFen-2, Sentinel-2, and LandSat-8 images, respectively

between 0.71 and 0.84, and 1.43 and 1.63 m, respectively. The results were similar for the Sentinel-2 and LandSat-8 images. These differences can be attributed to measurement errors and the accuracy of the tide correction, which should be considered when using the reference water depth data from different sources for validation [60].

D. Consistency of Bathymetric Estimates From Different Methods and Images

To verify the model consistency for each image, we calculated the mean of the bathymetric maps produced by all four models. The mean products were further compared with the corresponding single-model bathymetric maps. Fig. 8 illustrates the spatial distribution of the differences between the mean and single-model bathymetric maps. The highest consistency was observed for the LandSat-8 images, followed by the Sentinel-2 and GaoFen-2 images.

The inversion results of the four models are inconsistent for the GaoFen-2 images. For example, the deviation between the water depth estimated by BR_{BG} in the deep water areas around Shanhu and Ganquan islands and the mean values of the four models was less than -2 m; and that between the water depth estimated by RF_{BGR} in the shallow water area of the Lingyang Reef and the mean value was greater than 2 m. For the Sentinel-2 images, the depths estimated by BR_{BG} and SVR_{BGR} were significantly different from the mean bathymetric maps, especially in extremely shallow and deep water areas. The depths estimated by the four models were consistent with the mean bathymetric maps for the LandSat-8 images, and most of the deviations were between -1 and 1 m.

E. Difference Between Bathymetric Estimates From Different Methods and ALB Data

We combined ALB data as training data and the four models for inversion, using the obtained inversion results as *in situ* data for global water depth, *in situ* products were further compared with each model to explore the spatial difference of all inversion results. Fig. 9 shows the difference in spatial distribution between *in situ* data and single-model bathymetry. As shown in the figure, the difference between the Sentinel-2 image and *in situ* data is the smallest, while that between the GF-2 image and *in situ* data is the largest.

For GF-2 images, the overall inversion result largely deviated from the *in situ* data. In particular, the deviation of the BR_{BG} method in the deep water area of the three islands was generally greater than 2 m. The deviation in the shallow water area of the Antelope Reef and Shanhu Island reached 2 m. Compared with GF-2 images, the overall inversion results of Landsat-8 images were improved to a certain extent, but the inversion results using LB_{BGR} and BR_{BG} methods on the Antelope Reef also had partial regional deviations greater than 2 m. The overall deviation of Sentinel-2 images was relatively small, while that in the deep water area of the Ganquan Island and Coral Island using the BR_{BG} method was greater than 2 m.

V. Discussion

A. Shallow Water Bathymetry Based Only on Remote Sensing Data

ICESat-2 was not originally designed for marine applications and its trajectories have a limited global distribution. However, the use of a 532-nm laser and the high-accuracy of the altimetry give it great potential in shallow water bathymetry, topographic surveys, and related marine applications [26]. In this study, the bathymetric points from the spaceborne ICESat-2 LiDAR were used instead of *in situ* bathymetric points to train the four retrieval models. This approach utilizes the high-accuracy of ICESat-2 bathymetric points and the wide coverage of multispectral remote sensing images. This new approach means that bathymetric maps for shallow waters can be produced using only remotely sensed data from satellites, which provides a new perspective for shallow water bathymetry worldwide.

B. Influence of Tide and Refraction Corrections on ICESat-2 Bathymetric Points

Refraction and tide corrections are essential for nearshore bathymetry when using the ATLAS dataset and remote sensing images. The *in situ* measurements from the tide stations did not cover the acquisition times of all the multispectral images in this study, so tide corrections were performed using the tide model NAO.99b. The refraction effect that occurs at the air–water interface causes changes in the transmission speed and direction, which leads to the deviation of underwater photons (approximately 5 m for 20 m of water depth). Based on the results published by Parrish *et al.* [28], the sea surface was assumed to be flat, and the accuracy of the bathymetry improved significantly after refraction correction. We also conducted refraction correction in the study area. However, the assumption regarding the sea surface introduced some errors. Thus, further measures are required to improve the accuracy of the tide and refraction corrections, e.g., the employment of tide gauge data and refraction corrections based on sea wave simulations.

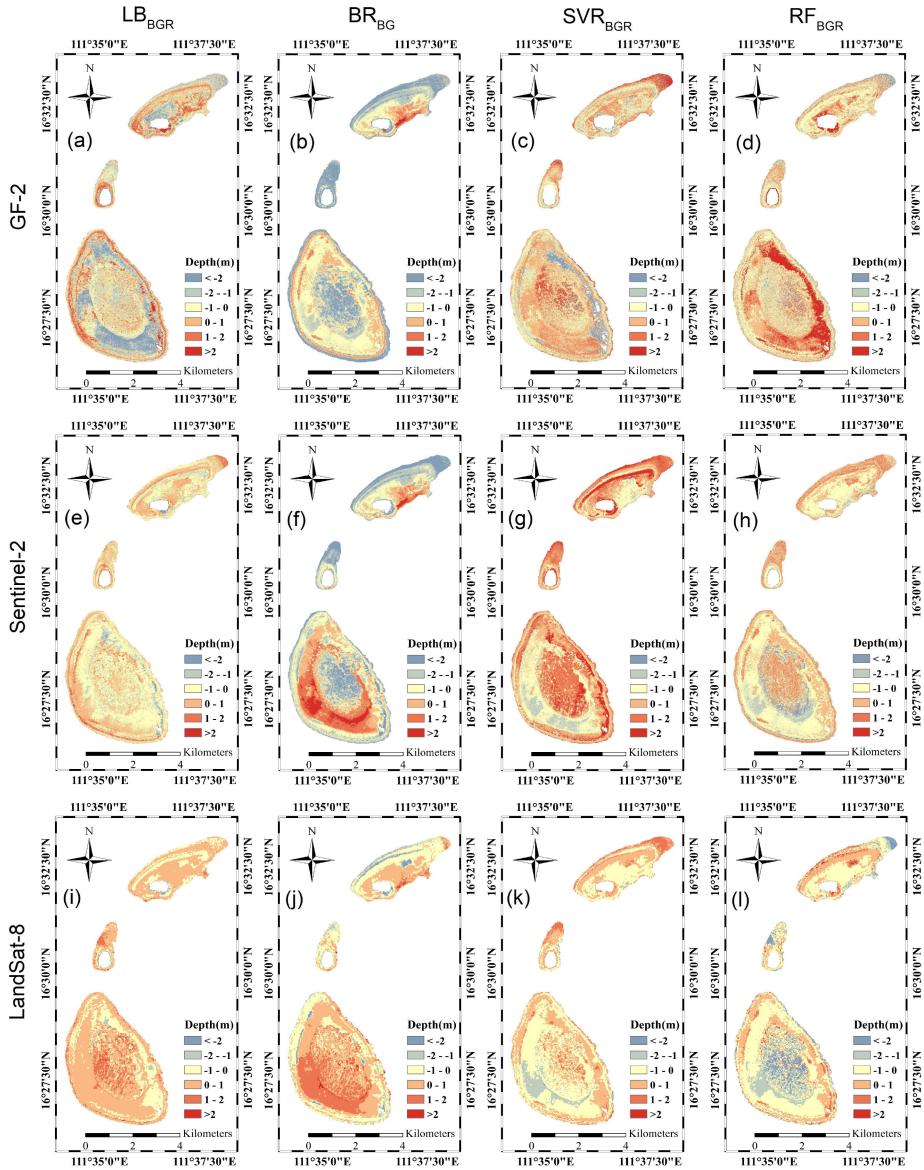

Fig. 8. Spatial distribution of differences between the mean and single-model bathymetric maps. (a)–(d) correspond to the spatial distribution of the differences between the LB_{BGR}, BR_{BG}, SVR_{BGR}, and RF_{BGR} models for the GaoFen-2 image. (e)–(h) and (i)–(l) are for the Sentinel-2 and LandSat-8 images, respectively.

C. Error of SDB

Image quality is affected by the lighting conditions, which correspond to the image acquisition time and the performance of the satellite sensor. Therefore, the process of atmospheric correction [61] and the removal of sun glint [62] is key to reliable bathymetric estimation. Although these corrections are performed during data preprocessing, the residuals cannot be neglected because they introduce errors to water depth estimations. Local water transparency, water column conditions, and bottom type also affect the estimation results depending on how well the *in situ* measurements cover all the bottom types and water quality conditions. Strict assumptions set to obtain higher model accuracy, typically lead to overfitting in machine learning algorithms [63]. The RF model in this study showed the best calibration accuracy, but the validation accuracy with respect to the reference data decreased considerably. Because the validation accuracy did not change significantly after changing the depth of the RF model, the validation accuracy of the RF model for the LandSat-8 data showed the most significant decrease. It can be inferred that overfitting of the RF model is caused by the small amount of data available after sampling. Therefore, the RF model constructed using ICESat-2 and multispectral images have poor generalization ability and is not suitable for migration to other data. To explore the effect of the corresponding relationship between photon resolution and image resolution on the performance of the inversion model, we used the mean-resampling method to sample the photon resolution to the same resolution as the multispectral image, so that only one photon is contained in a pixel. As given in Table V, this method improved the accuracy of the nonlinear model constructed based on SVR and RF, and slightly increased

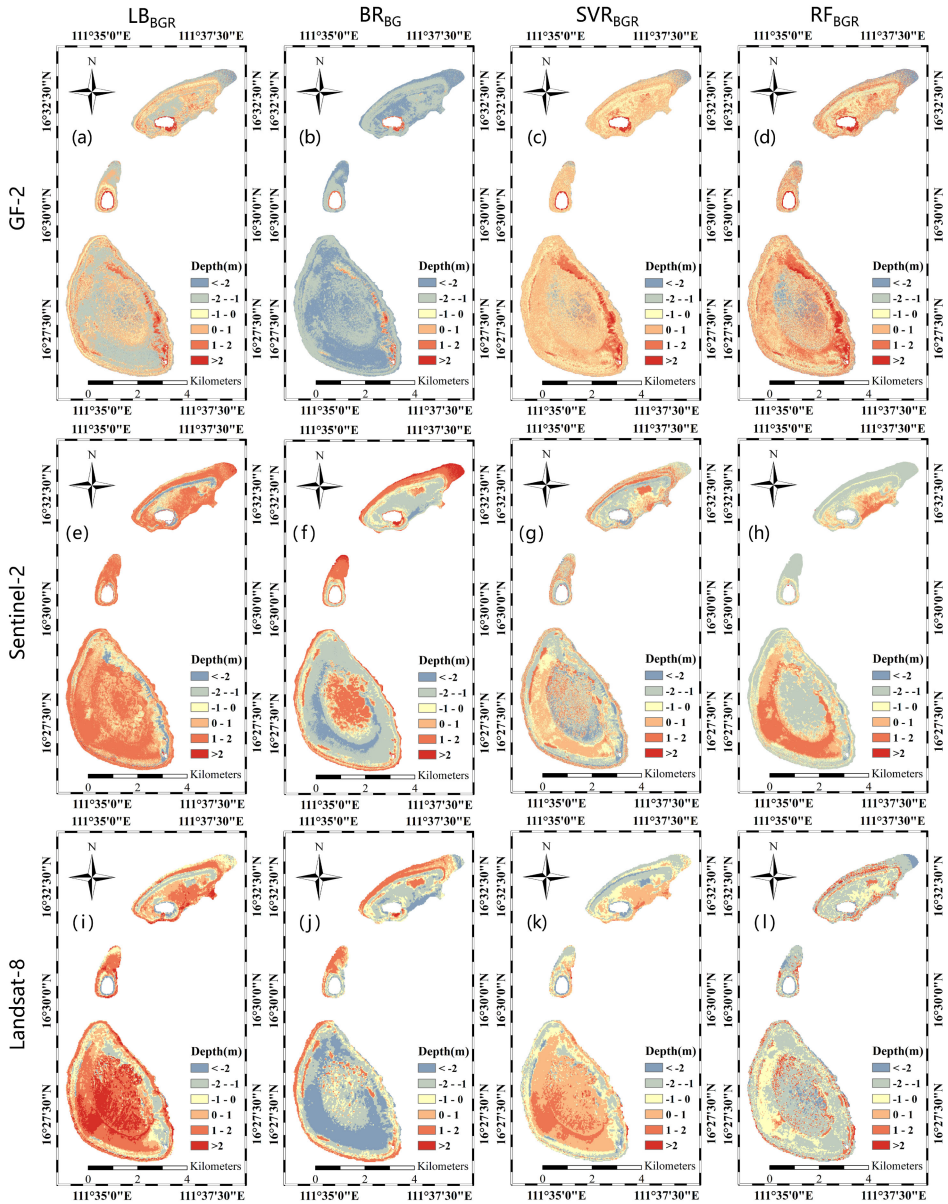

Fig. 9. Spatial distribution of differences between the *in situ* map and single-model bathymetric maps. (a)–(d) correspond to the spatial distribution of the differences between the LB$_{BGR}$, BR$_{BG}$, SVR$_{BGR}$, and RF$_{BGR}$ models for the GaoFen-2 image, while (e)–(h) and (i)–(l) show the same data for the Sentinel-2 and LandSat-8 images, respectively.

TABLE V
COMPARISON OF R^2 AND RMSE VALUES OF VALIDATION RESULTS FOR THREE MULTISPECTRAL IMAGES BEFORE AND AFTER SAMPLING

Images	LB_{BGR}				BR_{BG}				SVR_{BGR}				RF_{BGR}			
	Before		After		Before		After		Before		After		Before		After	
	R^2	RMSE	R^2	RMSE	R^2	RMSE	R^2	RMSE	R^2	RMSE	R^2	RMSE	R^2	RMSE	R^2	RMSE
GaoFen-2	0.69	1.71	0.71	1.63	0.67	2.12	0.72	1.61	0.80	1.60	0.84	1.43	0.69	1.63	0.81	1.58
Sentinel-2	0.88	1.08	0.90	0.94	0.83	1.22	0.87	1.12	0.85	1.12	0.89	0.97	0.83	1.51	0.88	1.31
LandSat-8	0.82	1.39	0.84	1.21	0.84	1.27	0.86	1.23	0.87	1.21	0.91	1.15	0.84	1.53	0.88	1.33

the accuracy of the linear model constructed using the LB and BR bands, which indicates that the resolution has a certain effect on the performance of the model [29]. Although resampling of photons improves the accuracy of the nonlinear model, it decreases the reliability of the nonlinear model, and after sample reduction, the RF model will exhibit overfitting, which must be addressed carefully.

VI. CONCLUSION

The bathymetric points acquired from the ICESat-2 data were combined with multispectral images to train two empirical models (the multiband and band ratio models) and two machine learning models (the SVR and RF models). Using these four models, a total of 12 shallow water bathymetric maps of three different images of the study area were generated. First, an adaptive variable ellipse filter was applied to eight tracks of the ATL03 data to extract the sea surface and underwater photons. Then, fraction correction was performed on the underwater photons to correct the water depth error.

Based on the two tracks, which overlapped to the northwest of Lingyang Reef, the bathymetric points of ICESat-2 were compared directly with the ALB reference data. The results

showed that the corrected seafloor photons of ICESat-2 had a significant correlation with the ALB profile, where $R^2 > 0.93$ and rmse < 0.52.

Second, six of the eight ATL03 data tracks were used as *a priori* measurements to train the four models, and two tracks were used as test data to assess their accuracy. The dual-band models constructed using blue and green bands were more accurate than those constructed using the other two bands. The detection capability of the GaoFen-2 satellite sensor in the blue band is significantly weaker than that of the Sentinel-2 and LandSat-8, so the inversion model constructed using the blue and green bands of GaoFen-2 was less accurate than that constructed using the blue and green bands of Sentinel-2 and LandSat-8.

The accuracy of the three-band models was slightly higher than that of the dual-band models. Overall, the machine learning models performed better than the empirical models.

The SVR_{BGR} model constructed using the Sentinel-2 data had the highest verification accuracy, with a mean R^2 and rmse of 0.90 and 1.16, respectively. Machine learning methods could fit the relationship between the ICESat-2 bathymetric points and the reflectance of the multispectral images better than the traditional empirical models, resulting in higher reliability and generalization capabilities.

The bathymetric methods developed in this study are based on multispectral images and bathymetric points using ICESat-2 data instead of *in situ* data. The result suggests that data for shallow water can be obtained on a global-scale using satellite-based remotely sensed data alone. This approach avoids the limitations of traditional methods, and provides practical solutions for water depth measurements in remote areas far from the continental shelf.

REFERENCES

[1] K. L. Brodie, B. L. Bruder, R. K. Slocum, and N. J. Spore, "Simultaneous mapping of coastal topography and bathymetry from a lightweight multicamera UAS," *IEEE Trans. Geosci. Remote Sens.*, vol. 57, no. 9, pp. 6844–6864, Sep. 2019.

[2] G. Simarro *et al.*, "The influence of camera calibration on nearshore bathymetry estimation from UAV videos," *Remote Sens.*, vol. 13, no. 1, 2021, Art. no. 150.

[3] A. Pacheco, J. Horta, C. Loureiro, and Ó. Ferreira, "Retrieval of nearshore bathymetry from Landsat 8 images: A tool for coastal monitoring in shallow waters," *Remote Sens. Environ.*, vol. 159, pp. 102–116, 2015.

[4] T. Mason, B. Rainbow, and S. McVey, "Colouring the 'white ribbon': Strategic coastal monitoring in the south–east of England," *Hydro Int.*, vol. 10, no. 4, pp. 19–21, 2006.

[5] J. X. Leon, S. R. Phinn, S. Hamylton, and M. I. Saunders, "Filling the 'white ribbon'– A multisource seamless digital elevation model for Lizard Island, northern Great Barrier Reef," *Int. J. Remote Sens.*, vol. 34, no. 18, pp. 6337–6354, 2013.

[6] T. Kutser, J. Hedley, C. Giardino, C. Roelfsema, and V. E. Brando, "Remote sensing of shallow waters– A 50 year retrospective and future directions," *Remote Sens. Environ.*, vol. 240, 2020, Art. no. 111619.

[7] Y. Jiang, Z. Yang, Z. Liu, and C. Yang, "High-resolution bottom detection algorithm for a multibeam echo-sounder system with a U-shaped array," *Acta Oceanologica Sinica*, vol. 37, no. 7, pp. 78–84, 2018.

[8] A. T. Kotilainen and A. M. Kaskela, "Comparison of airborne LiDAR and shipboard acoustic data in complex shallow water environments: Filling in the white ribbon zone," *Mar. Geol.*, vol. 385, pp. 250–259, 2017.

[9] M. Kim, V. Feygels, Y. Kopilevich, and J. Y. Park, "Estimation of inherent optical properties from CZMIL LiDAR," *Proc. SPIE*, vol. 9262, 2014, Art. no. 92620W.

[10] C. Wang, Q. Li, Y. Liu, G. Wu, P. Liu, and X. Ding, "A comparison of waveform processing algorithms for single-wavelength LiDAR bathymetry," *ISPRS Int. J. Geo Inf.*, vol. 101, pp. 22–35, 2015.

[11] R. Schwarz, G. Mandlburger, M. Pfennigbauer, and N. Pfeifer, "Design and evaluation of a full-wave surface and bottom-detection algorithm for LiDAR bathymetry of very shallow waters," *ISPRS Int. J. Geo Inf.*, vol. 150, pp. 1–10, 2019.

[12] Ł. Janowski, J. Tęgowski, and J. Nowak, "Seafloor mapping based on multibeam echosounder bathymetry and backscatter data using object-based image analysis: A case study from the Rewal site, the Southern Baltic," *Oceanological Hydrobiological Stud.*, vol. 47, no. 3, pp. 248–259, 2018.

[13] I. Caballero and R. P. Stumpf, "Retrieval of nearshore bathymetry from Sentinel-2A and 2B satellites in South Florida coastal waters," *Estuarine, Coastal Shelf Sci.*, vol. 226, 2019, Art. no. 106277.

[14] G. Casal, P. Harris, X. Monteys, J. Hedley, C. Cahalane, and T. McCarthy, "Understanding satellite-derived bathymetry using Sentinel 2 imagery and spatial prediction models," *GISci. Remote Sens.*, vol. 57, no. 3, pp. 271–286, 2020.

[15] A. P. Yunus, J. Dou, X. Song, and R. Avtar, "Improved bathymetric mapping of coastal and lake environments using Sentinel-2 and Landsat-8 images," *Sensors*, vol. 19, no. 12, 2019, Art. no. 2788.

[16] M. D. M. Manessa *et al.*, "Evaluating the performance of Lyzenga's water column correction in case-1 coral reef water using a simulated Wolrdview-2 imagery," *IOP Conf. Ser., Earth Environ. Sci.*, vol. 47, no. 1, 2016, Art. no. 12018.

[17] S. M. Adler-Golden, P. K. Acharya, A. Berk, M. W. Matthew, and D. Gorodetzky, "Remote bathymetry of the littoral zone from AVIRIS, LASH, and QuickBird imagery," *IEEE Trans. Geosci. Remote. Sens.*, vol. 43, no. 2, pp. 337–347, Feb. 2005.

[18] D. R. Lyzenga, N. P. Malinas, and F. J. Tanis, "Multispectral bathymetry using a simple physically based algorithm," *IEEE Trans. Geosci. Remote. Sens.*, vol. 44, no. 8, pp. 2251–2259, Aug. 2006.

[19] R. P. Stumpf, K. Holderied, and M. Sinclair, "Determination of water depth with high-resolution satellite imagery over variable bottom types," *Limnol. Oceanogr. Lett.*, vol. 48, no. 1, pp. 547–556, 2003.

[20] A. G. Dekker *et al.*, "Intercomparison of shallow water bathymetry, hydro-optics, and benthos mapping techniques in Australian and Caribbean coastal environments," *Limnol. Oceanogr. Methods*, vol. 9, no. 9, pp. 396–425, 2011.

[21] C. Cahalane, A. Magee, X. Monteys, G. Casal, J. Hanafin, and P. Harris, "A comparison of Landsat 8, rapideye and pleiades products for improving empirical predictions of satellite-derived bathymetry," *Remote Sens. Environ.*, vol. 233, 2019, Art. no. 111414.

[22] J. D. Hedley *et al.*, "Coral reef applications of Sentinel-2: Coverage, characteristics, bathymetry and benthic mapping with comparison to Landsat 8," *Remote Sens. Environ.*, vol. 216, pp. 598–614, 2018.

[23] G. Casal, X. Monteys, J. Hedley, P. Harris, C. Cahalane, and T. McCarthy, "Assessment of empirical algorithms for bathymetry extraction using Sentinel-2 data," *Int. J. Remote Sens*, vol. 40, no. 8, pp. 2855–2879, 2019.

[24] Y. Ma *et al.*, "Satellite-derived bathymetry using the ICESat-2 LiDAR and Sentinel-2 imagery datasets," *Remote Sens. Environ.*, vol. 250, 2020, Art. no. 112047.

[25] B. Smith *et al.*, "Land ice height-retrieval algorithm for NASA's ICESat-2 photon-counting laser altimeter," *Remote Sens. Environ.*, vol. 233, 2019, Art. no. 111352.

[26] T. Markus *et al.*, "The ice, cloud, and land elevation satellite-2 (ICESat-2): Science requirements, concept, and implementation," *Remote Sens. Environ.*, vol. 190, pp. 260–273, 2017.

[27] N. A. Forfinski-Sarkozi and C. E. Parrish, "Analysis of MABEL bathymetry in Keweenaw Bay and implications for ICESat-2 ATLAS," *Remote Sens.*, vol. 8, no. 9, 2016, Art. no. 772.

[28] C. E. Parrish, L. A. Magruder, A. L. Neuenschwander, N. Forfinski-Sarkozi, M. Alonzo, and M. Jasinski, "Validation of ICESat-2 ATLAS bathymetry and analysis of ATLAS's bathymetric mapping performance," *Remote Sens.*, vol. 11, no. 14, 2019, Art. no. 1634.

[29] A. Albright and C. Glennie, "Nearshore bathymetry from fusion of Sentinel-2 and ICESat-2 observations," *IEEE Geosci. Remote. Sens. Lett.*, vol. 18, no. 5, pp. 900–904, May 2021.

[30] P. Vinayaraj, V. Raghavan, and S. Masumoto, "Satellite-derived bathymetry using adaptive geographically weighted regression model," *Mar. Geodesy*, vol. 39, no. 6, pp. 458–478, 2016.

[31] D. R. Lyzenga, "Shallow-water bathymetry using combined LiDAR and passive multispectral scanner data," *Int. J. Remote Sens.*, vol. 6, no. 1, pp. 115–125, 1985.

[32] Y. Liu *et al.*, "An adaptive blended algorithm approach for deriving bathymetry from multispectral imagery," *IEEE J. Sel. Top. Appl. Earth Observ. Remote Sens.*, vol. 14, pp. 801–817, 2020, doi: 10.1109/JSTARS.2020.3034375.
[33] B. Cao, R. Deng, S. Zhu, Y. Liu, Y. Liang, and L. Xiong, "Bathymetric retrieval selectively using multi-angular high-spatial-resolution satellite imagery," *IEEE J. Sel. Top. Appl. Earth Observ. Remote Sens.*, vol. 14, pp. 1060–1074, 2021, doi: 10.1109/JSTARS.2020.3040186.
[34] N. A. Forfinski-Sarkozi and C. E. Parrish, "Active-passive spaceborne data fusion for mapping nearshore bathymetry," *Photogrammetric Eng. Remote Sens.*, vol. 85, no. 4, pp. 281–295, 2019.
[35] M. Awad and R. Khanna, "Support vector regression," in *Efficient Learning Machines*. Berlin, Germany: Springer, 2015, pp. 67–80.
[36] O. Mutanga, E. Adam, and M. A. Cho, "High density biomass estimation for wetland vegetation using Worldview-2 imagery and random forest regression algorithm," *Int. J. Appl. Earth Observ. Geoinformat.*, vol. 18, pp. 399–406, 2012.
[37] F. Tonion, F. Pirotti, G. Faina, and D. Paltrinieri, "A machine learning approach to multispectral satellite derived bathymetry," *ISPRS Int. J. Geo Inf.*, vol. 3, pp. 565–570, 2020.
[38] J.-Y. Zhang, J. Zhang, Y. Ma, A.-N. Chen, J. Cheng, and J.-X. Wan, "Satellite-derived bathymetry model in the arctic waters based on support vector regression," *J. Coastal Res.*, vol. 90, no. SI, pp. 294–301, 2019.
[39] N. Thomas *et al.*, "Space-borne cloud-native satellite-derived bathymetry (SDB) models using ICESat-2 and Sentinel-2," *Geophys. Res. Lett.*, vol. 48, no. 6, 2021, Art. no. e2020GL092170.
[40] Y. Chen, Z. Zhu, Y. Le, Z. Qiu, G. Chen, and L. Wang, "Refraction correction and coordinate displacement compensation in nearshore bathymetry using ICESat-2 LiDAR data and remote-sensing images," *Opt. Exp.*, vol. 29, no. 2, pp. 2411–2430, 2021.
[41] Y. Liu *et al.*, "Rapid estimation of bathymetry from multispectral imagery without in situ bathymetry data," *Appl. Opt.*, vol. 58, no. 27, pp. 7538–7551, 2019.
[42] A. Neuenschwander, S. Popescu, R. Nelson, D. Harding, K. Pitts, and J. Robbins, "ATLAS/ICESat-2 L3A land and vegetation height, version 2," ATL08 Data ProductBoulder, Colorado USANSIDC, National Snow and Ice Data Center, 2019. [Online]. Available: https://nsidc.org/data/ATL08/versions/2
[43] R. Kwok *et al.*, "ATLAS/ICESat-2 L3A sea ice height, version 1," *National Snow and Ice Data Center*, 2019. [Online]. Available: https://nsidc.org/data/ATL08/versions/2
[44] G. Dandabathula, M. Verma, P. Satyanarayana, and S. S. Rao, "Evaluation of ICESat-2 ATL08 data product: Performance assessment in inland water," *Eur. J. Environ. Sci.*, vol. 1, no. 3, 2020.
[45] M. W. Matthew *et al.*, "Atmospheric correction of spectral imagery: Evaluation of the FLAASH algorithm with AVIRIS data," in *Proc. Appl. Imagery Pattern Recognit. Workshop*, 2002, pp. 157–163.
[46] A. Collin *et al.*, "Statistical classification methodology of shoals 3000 backscatter to mapping coastal benthic habitats," in *Proc. IEEE Int. Geosci. Remote Sens. Symp.*, 2007, pp. 3178–3181.
[47] S. Peeri, J. V. Gardner, L. G. Ward, and J. R. Morrison, "The seafloor: A key factor in LiDAR bottom detection," *IEEE Trans. Geosci. Remote. Sens.*, vol. 49, no. 3, pp. 1150–1157, Mar. 2011.
[48] R. Narayanan, H. B. Kim, and G. Sohn, "Classification of shoals 3000 bathymetric LiDAR signals using decision tree and ensemble techniques," in *Proc. IEEE Toronto Int. Conf. Sci. Technol. Humanity*, 2009, pp. 462–467.
[49] Y. Tan, G. Zhou, X. Zhou, J. Wei, J. Chen, and H. Hu, "Overview of Chinese and American marine airborne LiDAR," *Int. Arch. Photogramm. Remote Sens. Spatial Inf. Sci.*, vol. 42, pp. 111–115, 2020.
[50] G. C. Guenther, W. J. Lillycrop, and J. R. Banic, "Future advancements in airborne hydrography," *Int. Hydrographic Rev.*, vol. 3, pp. 67–90, 2002.
[51] H. Zhao, Q. Zhang, R. Tu, and Z. Liu, "Determination of ocean tide loading displacement by GPS PPP with priori information constraint of NAO99b global ocean tide model," *Mar. Geodesy*, vol. 41, no. 2, pp. 159–176, 2018.
[52] L. Duncanson *et al.*, "Biomass estimation from simulated GEDI, ICESat-2 and NISAR across environmental gradients in Sonoma County, California," *Remote Sens. Environ.*, vol. 242, 2020, Art. no. 111779.
[53] Z. Pan, C. Glennie, C. Legleiter, and B. Overstreet, "Estimation of water depths and turbidity from hyperspectral imagery using support vector regression," *IEEE Geosci. Remote. Sens. Lett.*, vol. 12, no. 10, pp. 2165–2169, Oct. 2015.
[54] M. Diesing, S. L. Green, D. Stephens, R. M. Lark, H. A. Stewart, and D. Dove, "Mapping seabed sediments: Comparison of manual, geostatistical, object-based image analysis and machine learning approaches," *Continental Shelf Res.*, vol. 84, pp. 107–119, 2014.
[55] F. N. Spiess, C. D. Chadwell, J. A. Hildebrand, L. E. Young, G. H. Purcell, and H. Dragert, "Precise GPS/acoustic positioning of seafloor reference points for tectonic studies," *Phys. Earth Planet. Interiors*, vol. 108, no. 2, pp. 101–112, 1998.
[56] C. Flener, E. Lotsari, P. Alho, and J. Käyhkö, "Comparison of empirical and theoretical remote sensing based bathymetry models in river environments," *River Res. Appl.*, vol. 28, no. 1, pp. 118–133, 2012.
[57] B. Parsons and J. G. Sclater, "An analysis of the variation of ocean floor bathymetry and heat flow with age," *J. Geophys. Res.*, vol. 82, no. 5, pp. 803–827, 1977.
[58] R. Flower and A. Nicholson, "Relationships between bathymetry, water quality and diatoms in some hebridean lochs," *Freshwater Biol.*, vol. 18, no. 1, pp. 71–85, 1987.
[59] H. Bradner *et al.*, "Attenuation of light in clear deep ocean water," in *Proc. 2nd NESTOR Int. Workshop*, 1992, pp. 247–252.
[60] K. W. Hess, R. A. Schmalz, C. E. Zervas, and W. Collier, "Tidal constituent and residual interpolation (TCARI): A new method for the tidal correction of bathymetric data," 1999.
[61] I. Caballero and R. P. Stumpf, "Atmospheric correction for satellite-derived bathymetry in the Caribbean waters: From a single image to multi-temporal approaches using Sentinel-2A/B," *Opt. Exp.*, vol. 28, no. 8, pp. 11742–11766, 2020.
[62] F. Eugenio, J. Marcello, and J. Martin, "High-resolution maps of bathymetry and benthic habitats in shallow-water environments using multispectral remote sensing imagery," *IEEE Trans. Geosci. Remote. Sens.*, vol. 53, no. 7, pp. 3539–3549, Jul. 2015.
[63] M. R. Segal, "Machine learning benchmarks and random forest regression," 2004.

Xiaohan Zhang received the B.S. degree from the China University of Geosciences, Wuhan, China, where he is currently working toward the Ph.D. degree.

His research interests include machine learning, deep learning, unsupervised representation, and high-resolution remote sensing understanding.

Yifu Chen received the B.E. degree from Wuhan University, Wuhan, China, the M.E. degree from the Stuttgart University of Applied Science, Stuttgart, Germany, and the Ph.D. degree from Wuhan University.

He is currently a Teacher with the National Engineering Research Center for Geographic Information System, China University of Geosciences, Wuhan, China, where his work includes geometric calibration and characterization of satellite optical sensors, trajectory model research of push broom satellite, and the development of algorithms for generating digital surface models based on three-line optical images, using the techniques of photogrammetry and image processing.

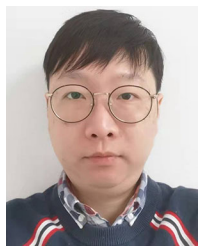

Yuan Le received the B.E. and Ph.D. degrees from the School of Remote Sensing and Information Engineering, Wuhan University, Wuhan, China.

Since 2015, he has been a Lecturer with the School of Geography and Information Engineering, China University of Geosciences, Wuhan. He has authored two books, 12 articles, and three inventions. His research interests include island reef and coastal environment, surface classification of islands, reefs and coastal zones, carbon cycle of terrestrial ecosystem in China, and full waveform and photon counting LiDAR technology.

Dongfang Zhang received the B.S. degree from the China University of Geosciences, Wuhan, China, where he is currently working toward the Ph.D. degree with the School of Computer Science.

His research focuses on the understanding of remote sensing images.

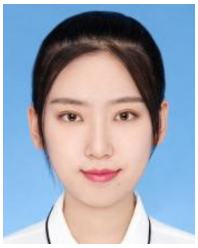

Qian Yan received the B.E. degree from South China Agricultural University, Guangzhou, China. She is currently working toward the M.A.Eng. degree in the China University of Geosciences, Wuhan, China.

Her research interests include algorithms for remote sensing inversion models, photon counting radar, and deep learning.

Yusen Dong received the Ph.D. degree from the China University of Geosciences, Wuhan, China.

He is currently an Associate Professor with the School of Computer Science, China University of Geosciences, where his work includes SAR interferometry for ground deformation and remote sensing survey of land and resources.

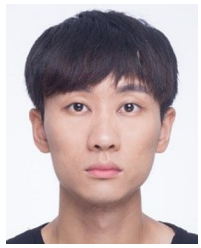

Wei Han received the B.S., M.S., and Ph.D. degrees from the China University of Geosciences, Wuhan, China.

He is currently an Associate Professor with the School of Computer Science, China University of Geosciences. His research interests include data management, high-performance computing, and high-resolution remote sensing image processing.

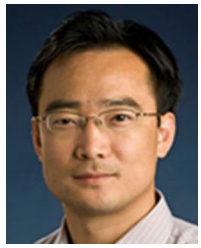

Lizhe Wang (Fellow, IEEE) received the B.E. and M.E. degrees from Tsinghua University, Beijing, China, and the D.E. degree *(magna cum laude)* from the University of Karlsruhe, Karlsruhe, Germany.

He is currently the Dean and "ChuTian" Chair Professor with the School of Computer Science, China University of Geosciences, Wuhan, China. His research interests include remote sensing data processing, digital Earth, and Big Data computing.

Prof. Wang is a Fellow of the IET and BCS and an Associate Editor of *Remote Sensing*, *International Journal of Digital Earth*, *ACM Computing Surveys*, IEEE TRANSACTIONS ON PARALLEL AND DISTRIBUTED SYSTEMS, and IEEE TRANSACTIONS ON SUSTAINABLE COMPUTING. He was the recipient of the Distinguished Young Scholars of NSFC, National Leading Talents of Science and Technology.